Medium-Entropy Engineering of Magnetism in Layered Antiferromagnet $Cu_xNi_{2(1-x)}Cr_xP_2S_6$

Dinesh Upreti, Rabindra Basnet, M. M. Sharma, Santosh Karki Chhetri, Gokul Acharya, Md Rafique Un Nabi, Josh Sakon, Mourad Benamara, Mansour Mortazavi, Jin Hu**

D. Upreti, R. Basnet, M. M. Sharma, S.K. Chhetri, G. Acharya, M.R.U. Nabi, J. Hu
Department of Physics, University of Arkansas, Fayetteville, Arkansas 72701, USA

R. Basnet, M. Mortazavi
Department of Chemistry & Physics, University of Arkansas at Pine Bluff, Pine Bluff, Arkansas 71603, USA

R. Basnet
Department of Physics, Morgan State University, Baltimore, MD, 21251, USA
rabindra.basnet@morgan.edu

M.R.U. Nabi, J. Hu
MonArk NSF Quantum Foundry, University of Arkansas, Fayetteville, Arkansas 72701, USA
jinhu@uark.edu

J. Sakon
Department of Chemistry & Biochemistry, University of Arkansas, Fayetteville, Arkansas 72701, USA

M. Benamara, J. Hu
Materials Science and Engineering Program, Institute for Nanoscience and Engineering, University of Arkansas, Fayetteville, Arkansas, 72701, USA

Keywords: Two-Dimensional Magnetism, Weak Ferromagnetism, Medium-Entropy Alloy, Aliovalent Substitution

Abstract

Antiferromagnetic van der Waals-type $M_2P_2X_6$ compounds provide a versatile material platform for studying two-dimensional magnetism and relavant phenomena. Establishing ferromagnetism in two-dimensional materials is technologically valuable. Though magnetism is generally tunable via a chemical way, it is challenging to induce ferromagnetism with isovalent chalcogen and bimetallic substitutions in $M_2P_2X_6$. Here, we co-substitute Cu^{1+} and Cr^{3+} for Ni^{2+} in $Ni_2P_2S_6$, creating $Cu_xNi_{2(1-x)}Cr_xP_2S_6$ medium-entropy alloys spanning a full substitution range (x = 0 to 1). Our findings reveal a unique evolution in crystal structure and magnetic phases that are distinct from traditional isovalent bimetallic doping, with Cu and Cr co-substitution enhancing ferromagnetic correlations and generating a weak ferromagnetic phase in intermediate compositions. This aliovalent substitution strategy offers a universal approach for tuning layered magnetism in antiferromagnetic systems, which along with the potential for light-matter interaction and high-temperature ferroelectricity, could enable multifunctional device applications.

1. Introduction

Tuning magnetic properties in layered magnets creates a pathway for a deeper understanding of magnetism in low dimensions and enlightens possible new routes to realize two-dimensional (2D) magnetic systems in real materials for spintronic applications[1–6]. Several strategies such as doping[7,8], high pressure[9–12] and electrostatic gating[3,13] have been implemented to tune magnetism in layered magnets. In addition, high- and medium-entropy alloys also offer an effective way to engineer magnetic properties. High-entropy alloys are defined as solid solutions containing more than five principal elements whereas medium-entropy alloys are considered as the intermediate between traditional alloys (with two principal elements) and high-entropy alloys[14,15]. Such high and medium-entropy alloys lead to enhanced configuration entropy. Since magnetic exchange interactions are highly dependent on elemental distribution in the lattice, this structural arrangement could significantly influence the magnetic properties. Therefore, owing to added complexity and parameter space, high- and medium-entropy alloys are expected to generate unusual magnetic orderings arising from competing magnetic interactions enabled by expanded degrees of freedom[16], which would result in additional functionalities for technology applications.

Single crystalline medium- or high-entropy layered magnets are barely explored. Recently, a few medium[17]- and high-entropy[18] layered antiferromagnetic (AFM) metal thiophosphates $M\mathrm{P}X_3$ (M = metal; X = chalcogen S or Se) compounds have been reported. These studies have revealed the modulation of magnetism under medium or high entropy environments in $M\mathrm{P}X_3$[17,18], but detailed investigation is still lacking. For various M and X, $M\mathrm{P}X_3$ compounds exhibit common structural characteristics[7,19–21] with metal atoms M arranged in a honeycomb lattice and sandwiched by P and X atoms, as shown in Figure 1a. In this structure, P forms P-P dimers perpendicular to the hexagonal metal plane. In each dimer, each P is bonded with three X to form $(\mathrm{P}_2X_6)^{4-}$ bipyramids filling the center of the M honeycomb lattice. Therefore, $M\mathrm{P}X_3$ is also referred to as $M_2\mathrm{P}_2X_6$, which will be used throughout this article.

Some $M_2P_2X_6$ materials exhibit robust AFM ordering from bulk to atomically thin limit[1,6,19,22–42]. This material family offers a broad avenue for technological applications because of the feasibility of obtaining atomically thin layers, enabling the fabrication of nanodevices and heterostructures-based electronics and spintronics. The $M_2P_2X_6$ compounds are mostly semiconductors with band gaps ranging from 1.3 to 3.5 eV, which makes them suitable for optoelectronic applications in a broad wavelength horizon[19,20]. In addition, other properties such as the unusual intercalation-reduction behavior, higher ionic conductivity, and unusual ferroelectricity of these materials expand their potential applications to Li-ion batteries[19,20,43,44], energy and data storage devices, and sensors[19,20]. Therefore, engineering magnetism and exploiting its coupling with electronic and optical properties would create novel phenomena and further enrich the technology applications.

The zero net moment of the AFM ground states of $M_2P_2X_6$ compounds complicates the detection of magnetism in the 2D limit and further hinders the integration of magnetism with other electronic and optical properties. Establishing ferromagnetism in $M_2P_2X_6$ would greatly unleash its potential as a spintronic platform. Earlier theoretical work has predicted the rise of ferromagnetism in $M_2P_2X_6$ via isovalent substitutions [45] and charge doping[46]. Experimentally, tuning magnetism in this material family is mostly based on bi-metallic [i.e., $(M_I^{2+}, M_{II}^{2+})P_2X_6$[7], where M_I and M_{II} are different metals][35,38,40,47–60] or bi-chalcogenide [i.e., $M_2P_2(S,Se)_6$][42,61–64] substitutions, and inter-layer intercalations[65–68]. In addition to diverse antiferromagnetism induced by various metal and chalcogen substitutions[35,38,40,42,47–59,61–64], signatures of ferromagnetism is only reported in Zn-substituted $Fe_2P_2S_6$[69] and Co-substituted $Ni_2P_2S_6$ [58], as well as guest species intercalated samples[65–67]. Even for the reported medium- and high-entropy $M_2P_2X_6$[17,18] that are more versatile due to their composition tunability, a ferromagnetic (FM) ground state is still absent. Most of the recent metal substitution studies adopt an isovalent substitution strategy[35,38,40,47–60]. In addition, a new metal substitution strategy has been adopted, in which the divalent M^{2+} ions in $M_2P_2X_6$ are fully replaced by an equal fraction of

monovalent M'^{1+} (M = Cu or Ag) and trivalent M''^{3+} (M'' = V or Cr) ions to form quaternary compounds $M'^{1+}M''^{3+}P_2X_6$, such as (Cu,Ag)(V,Cr)P_2X_6[70–78]. While these compounds have been discovered a long time ago[72,74–76], there have been very few studies on magnetism[70–72,74–77]. Though the ground states are still AFM, FM states have been realized by applying a magnetic field of around 6 T in $CuCrP_2S_6$[70,71] and $AgCrP_2Se_6$[78]. Such a polarization field is much lower than the rather high field (~ 35 T) needed to achieve a fully polarized FM state in a monometallic $Fe_2P_2S_6$[39]. It is worth noting that such an AFM to FM transition under a relatively weak field is commonly observed in Cr-based layered antiferromagnets[79–81], which has been ascribed to a weak AFM coupling between Cr^{3+} moments within an A-type magnetic ordering and a small magnetic anisotropy because of a lack of orbital degeneracy for Cr^{3+} (d^3) ion[70,71,80,82,83]. More interestingly, with the inclusion of another trivalent V^{3+}, $AgVP_2Se_6$ is reported to exhibit a robust FM ground state from bulk to atomically thin limit [77]. These results suggest that the trivalent Cr^{3+} and V^{3+} ions may favor FM correlation in $M_2P_2X_6$.

Inspired by these studies, here we report a new doping strategy in $M_2P_2X_6$ to engineer magnetism and promote ferromagnetism, which involves the simultaneous mixing of mono-, di-, and tri-valent metal ions. We successfully performed Cu^{1+} and Cr^{3+} substitutions for two Ni^{2+} in $Ni_2P_2S_6$ to form $Cu_xNi_{2(1-x)}Cr_xP_2S_6$ ($0 \le x \le 1$) leading to a wide range of medium-entropy compositions. Our work reveals a smoother evolution of AFM phases with substitution in $Cu_xNi_{2(1-x)}Cr_xP_2S_6$ as compared to traditional bimetallic substitution in $M_2P_2X_6$. The intermediate $Cu_xNi_{2(1-x)}Cr_xP_2S_6$ compositions $0.32 \le x \le 0.80$ exhibit a weak FM phase at low temperatures, which is likely attributed to the FM component of canted moments. The Cu and Cr (Cu+Cr) co-substitution in $Ni_2P_2S_6$ enhances FM correlation, which is manifested by the field-driven moment polarization and systematic rise of saturation moment that has been extremely challenging in $M_2P_2X_6$. Such aliovalent substitution and medium-entropy engineering provide an efficient approach to tuning layered magnets, creating a diverse landscape of new properties for implementation in device applications.

2. Results and discussion

Cr-based layered magnets exhibit robust magnetic orders in the 2D limit[84–88] and host great potential for applications in spintronic and multifunctional heterostructures. However, the study of Cr-based $M_2P_2X_6$ compounds is surprisingly limited. So far, only $Cr_2P_2Se_6$[89] and $Cr_{4/3}P_2S_6$[90] have been reported while the stoichiometric $Cr_2P_2S_6$ has not been experimentally realized. The $Cr_2P_2S_6$ phase is difficult to stabilize due to a weaker Cr-S covalency, favoring 3+ valence for Cr instead of the 2+ metal valence expected in $M_2P_2X_6$[91]. Substitution of 3+ ions for the M^{2+} in $M_2P_2X_6$ is challenging and sometimes causes strong metal ion vacancy as seen in $V_{2x}P_2S_6$ ($x = 0.78$[92,93] and 0.9[94]) that possess both V^{2+} and V^{3+} ions. This explains the recently reported Cr substitution of only up to 9% in $Ni_2P_2S_6$[95] which is contrary to a much higher substitution of other bi-valent metals like Mn, Fe, Co, Mg, etc. in $Ni_2P_2S_6$[38,40,53,54,57–59,96]. This chemical valence difference can be compensated by replacing bi-valent M^{2+} ions with mono- and di-valent metal ions, such as quaternary compounds $AgCrP_2(S,Se)_6$ and $CuCrP_2(S,Se)_6$[70,71,73,78]. Inspired by this idea, we successfully co-substitute Cu and Cr in $Ni_2P_2S_6$. As shown in the images in the right panel of Figure 1b, our extensive crystal growth effort (see Experimental Section) has yielded a wide range of single crystalline $(Cu,Ni,Cr)_2P_2S_6$ medium-entropy alloys. Composition analyses (see Experimental Section) by energy-dispersive *x*-ray spectroscopy (EDS) reveal nearly equal Cu and Cr substitutions for Ni in our crystals, i.e., substituting two Ni^{2+} by one Cu^{1+} and one Cr^{3+}, as summarized in Table 1. Therefore, the composition is represented as $Cu_xNi_{2(1-x)}Cr_xP_2S_6$, where x represents Cu or Cr content. Additionally, different single crystal pieces can exhibit varying compositions, even when grown with the same nominal composition. However, each piece of crystal displays compositional homogeneity. Therefore, the reported properties are reliable and accurately reflect the measured compositions. As expected, full substitution leads to $CuCrP_2S_6$[70,71]. As discussed above, the

enhanced Cr content is expected to induce and stabilize ferromagnetism, which is the goal of this study.

Table 1: Nominal elemental compositions of the source materials and the actual compositions of the obtained crystals determined by EDS for $Cu_xNi_{2(1-x)}Cr_xP_2S_6$.

Nominal *x*	**EDS composition**	***x* = (Cu+Cr)/2**
0	$Ni_{2.00}P_{1.99}S_{5.86}$	0
0.20	$Cu_{0.16}Ni_{1.69}Cr_{0.15}P_{1.93}S_{6.02}$	0.16
0.40	$Cu_{0.33}Ni_{1.46}Cr_{0.31}P_{1.95}S_{5.98}$	0.32
0.60	$Cu_{0.40}Ni_{1.31}Cr_{0.39}P_{1.92}S_{5.99}$	0.40
	$Cu_{0.45}Ni_{1.18}Cr_{0.47}P_{2.01}S_{5.85}$	0.46
	$Cu_{0.60}Ni_{0.81}Cr_{0.59}P_{1.99}S_{5.89}$	0.60
0.80	$Cu_{0.70}Ni_{0.58}Cr_{0.72}P_{1.91}S_{5.97}$	0.70
	$Cu_{0.82}Ni_{0.37}Cr_{0.81}P_{2.01}S_{5.98}$	0.80
0.90	$Cu_{0.94}Ni_{0.12}Cr_{0.94}P_{1.93}S_{5.88}$	0.94
1	$Cu_{0.97}Cr_{1.03}P_{1.88}S_{5.91}$	1

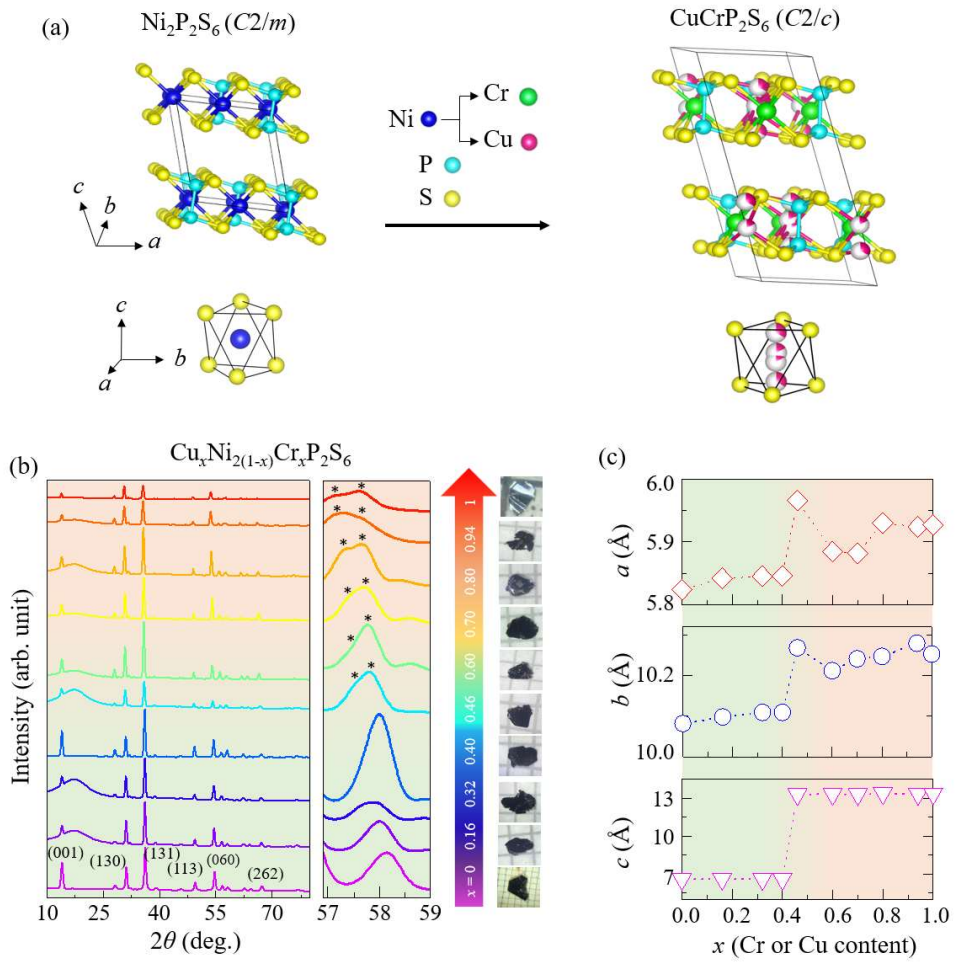

Figure 1. (a) Top: Crystal structures of $Ni_2P_2S_6$ and $CuCrP_2S_6$. Bottom: location of Ni ion in $Ni_2P_2S_6$ and Cu ion in $CuCrP_2S_6$ at room temperature. At room temperature, Cu atoms in $CuCrP_2S_6$ partially occupy multiple sites, as indicated by the partially filled magenta spheres. (b) X-ray diffraction for $Cu_xNi_{2(1-x)}Cr_xP_2S_6$ ($0 \le x \le 1$). Left panel: XRD data for all the samples from 10° to 80°; Middle panel: zoomed 2θ range between 57° to 59°; Right panel: the optical microscope images of single crystals for all the compositions from $x = 0$ to 1. (c) Composition dependence of lattice parameters a, b, and c in $Cu_xNi_{2(1-x)}Cr_xP_2S_6$. Different colored regions in (b) and (c) represent different crystal structures. The green color denotes the $Ni_2P_2S_6$ -type structure with a space group $C2/m$; the orange color denotes the $CuCrP_2S_6$-type structure with a space group $C2/c$.

Successful Cu and Cr substitutions in $Ni_2P_2S_6$ are further confirmed by the evolution of crystal structure probed by *x*-ray diffraction (XRD), which was performed on powdered samples obtained by grinding single crystals with well characterized compositions. Although the XRD patterns for all $Cu_xNi_{2(1-x)}Cr_xP_2S_6$ samples look similar in the left panel of Figure 1b, a systematic peak shift and splitting is observed, which is better seen in the middle panel of Figure 1b that displays XRD peaks between 57° and 59°. To obtain deeper insight into the structure evolution, we have performed Rietveld refinement (Figure S1, Supporting Information). The refinement confirms that the substitution occurs with two bi-valent Ni^{2+} being replaced by one mono-valent Cu^{1+} and one tri-valent Cr^{3+}. Furthermore, samples are found to adopt the $Ni_2P_2S_6$-type structure for compositions up to $x = 0.40$, with a slight expansion in lattice constants *a* and *b* as summarized in Figure 1c. This can be attributed to the larger average size of Cu^{1+} and Cr^{3+} as compared to Ni^{2+} and explains the systematic low-angle XRD peak shift up to $x = 0.40$ shown in the middle panel of Figure 1b. Increasing Cu and Cr amount to $x = 0.46$ causes a structural transition from the $Ni_2P_2S_6$-type to the $CuCrP_2S_6$-type. The structure differences between such two structures are shown in Figure 1a. The metal atoms in both $Ni_2P_2S_6$ and $CuCrP_2S_6$ organize in a similar honeycomb arrangement in the *ab*-plane when viewed along the *c*-axis[70,97], which makes the two structures hardly distinguishable. However, as depicted in the right panel of Figure 1a, in $CuCrP_2S_6$, the Cr^{3+} ions are located in the center of each sandwich layer, whereas the Cu^{1+} ions are off-centered along the *c*-axis at room temperature[70,71,97]. Moreover, Cu atoms have been found to exhibit positional and occupational disorders at room temperature[70], showing vacancies[70] as represented by the partially filled magenta spheres in the figure. As a result, the *c*-axis is nearly doubled in $CuCrP_2S_6$ [c = 13.360(8) Å] as compared to that of $Ni_2P_2S_6$ [6.616(3) Å][70,71,97]. Hence in our $Cu_xNi_{2(1-x)}Cr_xP_2S_6$, with increasing Cu and Cr co-substitution from $x = 0.4$ to 0.46, the doubling of c-axis [from 6.620(5) Å to 13.315(5) Å] as well as the sudden increases in *a* and *b* (Figure 1c) signature the structure transition from the $Ni_2P_2S_6$-type to the $CuCrP_2S_6$-type. Accompanied with the

structure transition is the symmetry reduction from a $C2/m$ space group to a $C2/c$ one, which explains the XRD peak splitting for $x \geq 0.46$ denoted by asterisks in the middle panel of Figure 1b. Therefore, though it is challenging to identify substitutions using cross-sectional transmission electron microscope imaging (Supporting Information) owing to the close atomic numbers of Cr, Ni, and Cu, our structure analysis using XRD provide strong evidence for the proposed aliovalent substitution scenario.

In $M_2P_2X_6$ compounds, isovalent metal-substituted compounds[35,38,40,47–59] are generally considered to exhibit a random distribution of substituted metal ions within the honeycomb network. Quaternary $(M'^{1+}M''^{3+})_2P_2X_6$ compounds have been proposed to show ordering due to the weaker repulsive coulomb interactions and substantial size differences between the mono- and tri-valent ions[73]. For example, Ag^{1+} and $(V \text{ or } Cr)^{3+}$ ions in $Ag(V,Cr)P_2X_6$ (X = S and Se)[72,73,77,78] form zig-zag chains, while in $CuCrP_2S_6$, Cu^{1+} and Cr^{3+} ions occupy separate layers[70]. Consequently, as the concentrations of Cu^+ and Cr^{3+} increase in $Cu_xNi_{2(1-x)}Cr_xP_2S_6$, the metal network should transit from a $Ni_2P_2S_6$-type to a $CuCrP_2S_6$-type structure. Except for the two end compounds $Ni_2P_2S_6$ and $CuCrP_2S_6$, the substituted metal ions likely form random distribution as expected in isovalent metal-substituted compounds. Therefore, this combination of Cu, Ni, and Cr creates a single solid solution phase with enhanced configurational entropy, classified as a medium-entropy alloy with three principal elements. In addition, chemical short-range order, which is characterized by the slight deviation of the atomic distribution from the perfect random distributions but does not strongly affect the strongly enhanced configuration entropy, has been discovered in other medium-entropy alloys[99,100]. It likely exists in $Cu_xNi_{2(1-x)}Cr_xP_2S_6$ and together with enhanced entropy may contribute to the modification of magnetism[7].

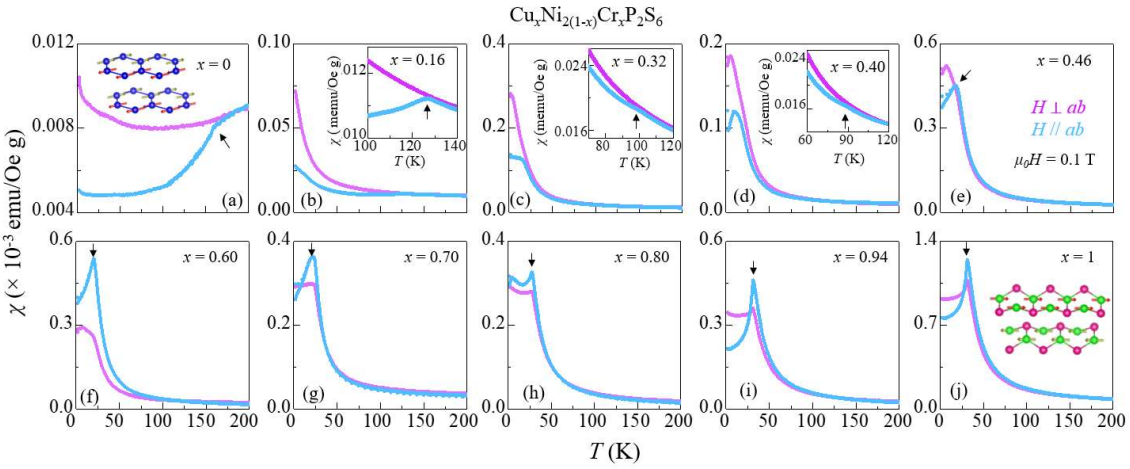

Figure 2. Temperature dependence of susceptibility (χ) for $Cu_xNi_{2(1-x)}Cr_xP_2S_6$ ($0 \leq x \leq 1$) samples measured with in-plane ($H//ab$, blue) and out-of-plane ($H \perp ab$, magenta) magnetic fields of 0.1 T. Insets in (a) and (j) show magnetic structures of the end compounds $x = 0$ and 1, respectively. Insets in (b), (c), and (d) show zoom-in view of low-temperature susceptibility to identify magnetic transitions. The black arrow in each panel denotes the AFM transition temperature T_N.

As the goal of this study is to induce ferromagnetism in $M_2P_2X_6$, to investigate the evolution of magnetic properties in medium-entropy $Cu_xNi_{2(1-x)}Cr_xP_2S_6$, we have measured the temperature dependence of susceptibility (χ) under in-plane ($H//ab$) and out-of-plane ($H \perp ab$) magnetic fields of $\mu_0 H$ = 0.1 T. The two end compounds $Ni_2P_2S_6$ ($x = 0$)[22,26,38,40,57,59,63] and $CuCrP_2S_6$ ($x = 1$)[70,71,75,97,98] have been found to possess a C-type zig-zag[26] and A-type[75,97] AFM structures below $T_N \approx 155$ K and 32 K, respectively, as denoted by black arrows in **Figure 2**a and 2j. In C-type zig-zag AFM structures, magnetic moments within each plane form zig-zag chains with adjacent chains arranged antiferromagnetically (Figure 2a, inset), while in A-type AFM structures, magnetic moments within each layer are aligned ferromagnetically, with moments in adjacent layers forming an antiferromagnetic alignment (Figure 2j, inset). Such in-

plane FM coupling in $CuCrP_2S_6$ might be associated with the significantly reduced T_N and low critical field (~6T) [70,71] for polarizing the AFM moments due to the competition between FM and AFM correlations. As illustrated in insets of Figure 2a and 2j, both end compounds have been reported to exhibit magnetic easy axes aligned within or near the basal plane[26,70,71], which can also be inferred from the magnetization measurements as will be shown later. Owing to their distinct magnetic structures, the magnetic exchange interactions are different. In $Ni_2P_2S_6$, the dominant third nearest-neighbor interaction J_3 is AFM though much weaker FM interactions (nearest-neighbor interaction J_1 and inter-layer interaction J_c) also exist[101,102]. On the other hand, despite the AFM ground state in $CuCrP_2S_6$, the magnetic order is governed by intra-layer FM interactions while inter-layer AFM interactions are rather weak[97]. Such distinct magnetic interactions in these compounds are in line with their different paramagnetic (PM) to AFM transition behaviors in susceptibility measurements. As shown in Figure 2a, susceptibility for $Ni_2P_2S_6$ lacks a sharp peak at T_N but exhibits a broad hump just above T_N in $\chi_{//}$, which has been ascribed to the short-range magnetic correlations above T_N[26,40,57,63]. In this case, the PM to AFM transition T_N can be estimated by the rise of anisotropy between in-plane ($\chi_{//}$) and out-of-plane ($\chi_{\perp}$) susceptibility measured under $H//ab$ and $H \perp ab$ respectively, where $\chi_{//}$ should be smaller than $\chi_{\perp}$ below T_N due to the in-plane moment orientation [26,38,40,57,59,63]. In $CuCrP_2S_6$[70,71], however, it exhibits a sharp AFM transition. Providing that the broad hump above T_N is believed to be associated with the short-range magnetic correlations before the establishment of long-range order[25], it is likely that the presence of Cu breaks such short-range correlation between Cr moments. Despite an in-plane magnetic easy axis (Figure 2j, inset)[70,71] similar to $Ni_2P_2S_6$[26], the A-type magnetic structure leads to a more pronounced susceptibility peak at T_N in $\chi_{//}$ than $\chi_{\perp}$ for $CuCrP_2S_6$.

The sharp difference in susceptibility transition between $Ni_2P_2S_6$ and $CuCrP_2S_6$ can be adopted as an indicator to understand the evolution of magnetism in $Cu_xNi_{2(1-x)}Cr_xP_2S_6$. As

shown in Figure 2b-2d, for samples close to the $Ni_2P_2S_6$ end (x = 0.16-0.40), susceptibility upturns develop below T < 50 K. At high temperatures, $\chi_\perp$ is essentially featureless but $\chi_{//}$exhibits a small kink, as indicated by the arrows. Above such kink temperature, $\chi_{//}$ and $\chi_\perp$ overlap. Such behavior resembles $Ni_2P_2S_6$-type susceptibility, i.e., relatively broad peak in $\chi_{//}$ and absence of a clear feature in $\chi_\perp$ at T_N. Therefore, we define such susceptibility kink as AFM transition for these substituted samples up to x = 0.4. This weak susceptibility feature disappears upon further increasing the Cu and Cr contents. Instead, the well-defined susceptibility peaks start to appear for $x \geq 0.46$, which is reminiscent of that of pristine $CuCrP_2S_6$[70,71] and implies the gradual development of $CuCrP_2S_6$-type AFM phase. Hence, the magnetic phases in these two composition regimes below and above x = 0.40 may be categorized as $Ni_2P_2S_6$-type and $CuCrP_2S_6$-type AFM phases, which are denoted as AFM_1 and AFM_2 respectively. Moreover, it is worth noting that the structure change also occurs above x = 0.40 as mentioned above.

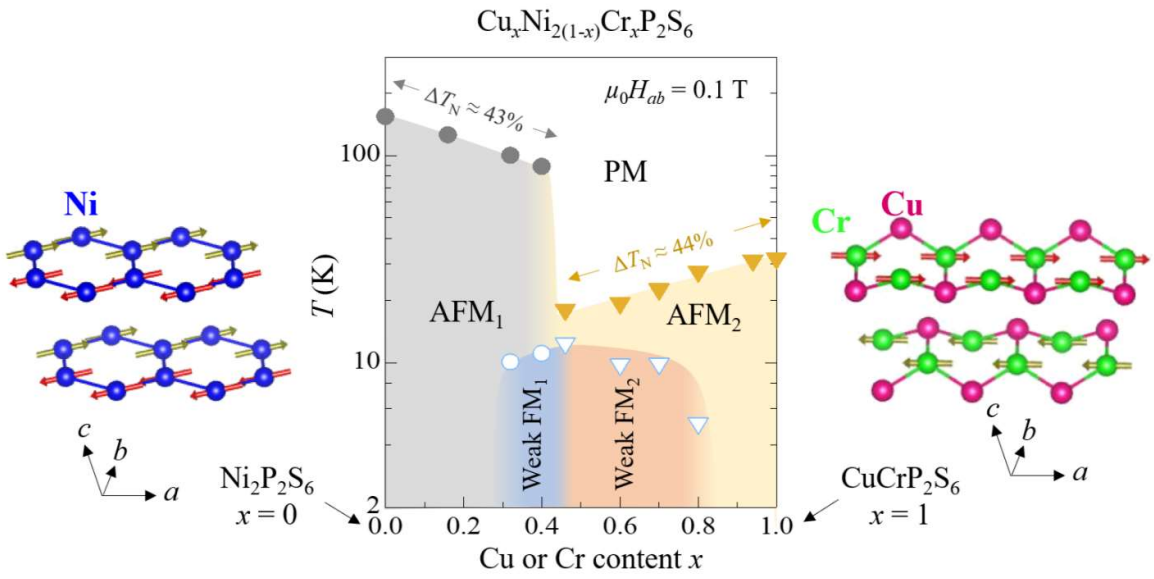

Figure 3. The magnetic phase diagram for $Cu_xNi_{2(1-x)}Cr_xP_2S_6$ ($0 \leq x \leq 1$) showing evolution of magnetic phases with doping and temperature, established based on magnetization measurements under in-plane magnetic field of 0.1 T. The magnetic structures of pristine

$Ni_2P_2S_6$ (x = 0) and $CuCrP_2S_6$ (x = 1) are presented on the sides of the phase diagram and denoted by AFM_1 (grey color) and AFM_2 (yellow color) in the phase diagram, respectively. Weak FM_1 (blue color) and weak FM_2 (orange color) phases, for intermediate compositions $0.32 \leq x \leq 0.40$ and $0.46 \leq x \leq 0.80$ within the AFM_1 and AFM_2 phases regime respectively, are defied using low-temperature ZFC and FC irreversibility.

The magnetic structure evolution with (Cu+Cr) co-substitution leads to significant modifications in magnetic exchange interactions, which contribute to the non-monotonic behavior of the magnetic ordering temperature, T_N, shown in the phase diagram in Figure 3. The T_N trend shows a systematic decrease in the AFM_1 region ($0 \leq x \leq 0.40$), followed by an abrupt drop at x = 0.46, and then a steady increase in the AFM_2 region. Aside from the sudden drop, T_N evolves nearly linearly with composition. The minimum T_N near x = 0.5, where nearly half of Ni is replaced by equal amounts of Cr and Cu, mirrors trends in isovalent substituted bimetallic $(M_I^{2+}, M_{II}^{2+})P_2X_6$ compounds, which has been attributed to the magnetic frustrations due to mixing magnetic ions in the honeycomb lattice plane[35,38,40,52,56]. However, the sudden T_N drop from x = 0.40 to 0.46 in our trimetallic $Cu_xNi_{2(1-x)}Cr_xP_2S_6$ sharply contrasts with the smooth evolution of T_N in bimetallic ones, indicating a sharp phase boundary between AFM_1 and AFM_2 phases in $Cu_xNi_{2(1-x)}Cr_xP_2S_6$. The coinciding structural change in this composition range may correspond to substantial modifications in exchange interactions between the two distinct metal sublattices (side panels in Figure 3). In insulating $M_2P_2X_6$ systems, magnetic properties are determined by magnetic exchange interactions and single-ion anisotropy, as described by the Heisenberg model[7,19–21]. In pristine $Ni_2P_2S_6$, the magnetic interactions are governed by a dominant third-nearest-neighbor AFM interaction J_3 within the *ab*-plane[101]. Due to Ni^{2+} (d^8) ions having filled lower three-fold degenerate t_{2g} orbitals under octahedral crystal fields, the direct exchange is absent[101], and magnetic interactions occur via superexchange pathways through non-magnetic S atoms. With (Cu+Cr) co-substitutions, AFM

J_3 most likely attenuates because Cr^{3+} (d^3) ions favor FM interactions, as evidenced by the dominant in-plane FM correlations of the A-type AFM structure in the end compound $CuCrP_2S_6$[97]. As a consequence, the attenuation of J_3 should contributes to the reduction of T_N. Furthermore, magnetic interaction modifications may be especially intense near the AFM_1-AFM_2 phase boundary due to the strong competition between these phases. Consequently, when both crystal and magnetic structures shift to $CuCrP_2S_6$-type at $x \sim 0.40$, T_N drops sharply across the phase boundary. Nevertheless, the T_N variation within each phase is relatively mild and symmetric. From $x = 0$ to 0.40, T_N reduces linearly to ~43%, while for $x = 1$ back to 0.46, it similarly drops to ~44%, as shown in Figure 3. This symmetric T_N evolution is distinct from bimetallic systems such as $(Ni_{1-x}Mn_x)_2P_2S_6$[36,38,103] and $(Fe_{1-x}Mn_x)_2P_2Se_6$[104], which exhibit asymmetrical T_N drops. The smooth and symmetric T_N trend in $Cu_xNi_{2(1-x)}Cr_xP_2S_6$ might indicate a relatively smoother disturbance by dopant in this material system, before triggering structure change between $x = 0.40$ and 0.46, possibly associated with the doping to different metal networks enforced by the different structure of end compounds. Additionally, with the suppression of magnetic exchange upon substitution as discussed above, the role of single ion anisotropy becomes relatively significant, consequently affecting the magnetic structure. For example, in $(Ni_{1-x}Mn_x)_2P_2S_6$, with reduced single ion anisotropy by increasing Mn content, magnetic structure changes from in-plane zig-zag ($Ni_2P_2S_6$) to out-of-plane Néel-type ($Mn_2P_2S_6$) that strongly affects the spin-flop transition[38] at around $x = 0.75$[103]. Similar behavior is seen in Ising-type $Fe_2P_2Se_6$, where heavy Mn substitution to 90% reorients the magnetic easy axis close to the in-plane direction[104].

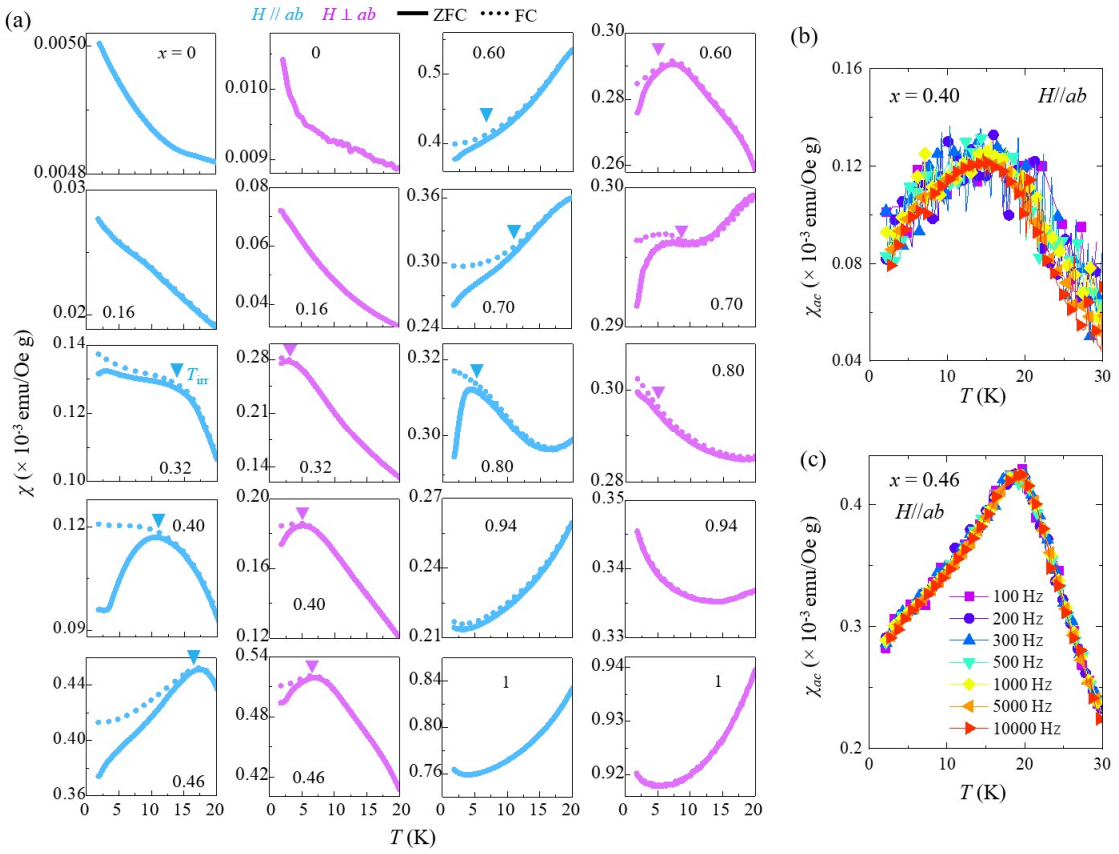

Figure 4. (a) Low-temperature zero-field cooling (ZFC; solid lines) and field-cooling (FC; dashed lines) susceptibility (χ) for $Cu_xNi_{2(1-x)}Cr_xP_2S_6$ ($0 \leq x \leq 1$) samples under in-plane (*H//ab*, blue) and out-of-plane ($H \perp ab$, magenta) magnetic fields of $\mu_0 H = 0.1$ T. The solid triangles denote the onset temperature T_{irr} of ZFC and FC irreversibility. (b-c) Temperature dependence of AC-susceptibility (χ_{ac}) for $x = 0.40$ (b) and 0.46 (c) samples under an in-plane AC field of 10 Oe at different frequencies from 100 Hz to 10,000 Hz. The same color code is used in (b) and (c).

Cu^{1+}, Ni^{2+}, and Cr^{3+} atomic arrangement could even be more influential in tuning magnetic interactions in compositions with substantial amounts of all three metal ions, which helps to realize an ideal medium-entropy environment. This is evident in the low-temperature susceptibility of intermediate compositions $0.32 \leq x \leq 0.80$. As shown in Figure 4a , both in-

plane $\chi_{//}$ and out-of-plane $\chi_{\perp}$ susceptibilities for these samples exhibit clear irreversibility between zero-field cooling (ZFC) and field-cooling (FC) measurements at temperatures (T_{irr}) well below T_N (solid triangles in Figure 4a), whereas other samples ($x \leq 0.16$ and ≥ 0.94) lack clear susceptibility irreversibility. The ZFC-FC bifurcation is more prominent in $\chi_{//}$ than $\chi_{\perp}$, which can be understood in terms of the in-plane or nearly in-plane moment orientation over the entire composition range. Such ZFC and FC irreversibility has been observed in pristine $Mn_2P_2S_6$ and attributed to a weak FM phase arising from field-induced moment canting in AFM sublattices[105]. The strongest irreversibility occurs in $x = 0.40$ and 0.46 samples where T_N is the lowest and competition is the strongest. It is not surprising that T_{irr} in $\chi_{//}$ consistently exceeds that in $\chi_{\perp}$ (Figure 4a), considering the in-plane easy axis. An in-plane easy axis for each composition is also evident in the field-dependent magnetization measurements at $T = 2$ K, as discussed below in Figure 5. With the determination of T_{irr} which is considered as the rise of the weak FM phase, the phase diagram in Figure 3 is further enriched with the inclusion of weak FM_1 and weak FM_2 phases, because they evolve from AFM_1 and AFM_2 phases characterized by different magnetic structures as discussed above.

The weak ferromagnetism arising from moment canting may stem from competing exchange interactions or crystal field effects[106] up on substitution. Additionally, the Dzyaloshinskii-Moriya interaction (DMI), which is a relativistic antisymmetric component of exchange interaction, arises with spin-orbit coupling. Although DMI generally requires certain lattice symmetries the same as the crystal field effect, it is often used to explain noncollinear magnetic structures with canted moments[107], which can result in weak ferromagnetism even in centrosymmetric antiferromagnets[108]. Recent theoretical work[109] proposes, however, that weak ferromagnetism in centrosymmetric and noncentrosymmetric conventional antiferromagnets is absent. Instead, materials often deemed antiferromagnetic with weak

ferromagnetism are altermagnets. Therefore, the discovery of weak ferromagnetism in $Cu_xNi_{2(1-x)}Cr_xP_2S_6$ offers an additional platform to further clarify moment canting mechanisms.

In addition to the weak FM state, the irreversibility between ZFC and FC susceptibility also occurs with the development of a spin-glass (SG) state. In $M_2P_2X_6$, the spin-glass transition has been observed upon metal substitution[17,52], which can be clarified by the frequency dependence of AC susceptibility. Because of the slow spin dynamics for an SG system, the spin relaxation time becomes longer. When an external AC magnetic field with a driving frequency is applied, the spin dynamics are enhanced with the increasing frequency of the AC field, consequently raising the SG temperature (T_{SG}). In Figure 4b and 4c we present AC susceptibilities for x = 0.40 and 0.46 samples - the ones that show the strongest irreversibility (Figure 4a) - measured with varying frequencies from 100 to 10,000 Hz. The absence of a notable shift rules out the possibility of an SG state. This provides additional support for the development of the weak FM state discussed above. Furthermore, our results on aliovalent substituted $Cu_xNi_{2(1-x)}Cr_xP_2S_6$ are in stark contrast to the SG states seen in isovalent substituted bimetallic[52] and medium-entropy[17] $M_2P_2X_6$ compounds. Such difference could be attributed to the ordering, either long-range or chemical short-range, of Cu^{1+}, Ni^{2+}, and Cr^{3+} due to the structure characteristics of this solid solution system as stated above, which prevents spin freezing.

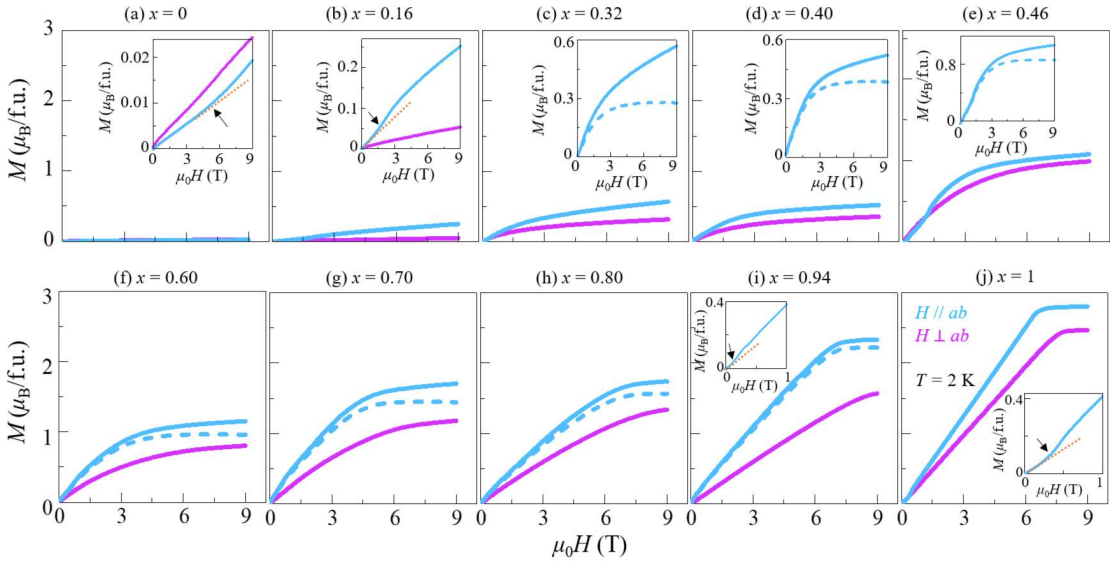

Figure 5. Field dependence of magnetization for $Cu_xNi_{2(1-x)}Cr_xP_2S_6$ ($0 \leq x \leq 1$) at T = 2 K measured with in-plane (H//ab, solid blue) and out-of-plane ($H \perp ab$, solid magenta) magnetic fields. Positive field scans from 0 to 9 T is shown as the negative field scan is symmetric, as shown in Figure S3 in Supporting Information. Insets in (a), (b), (i), and (j): Spin-flop transitions under H//ab for x = 0, 0.16, 0.94, and 1 samples characterized by the deviation from linear dependence (red dotted lines) and a super-linear field dependence for magnetization. The transition is denoted by black arrow in each inset. More complete information is provided in Figures S5 in Supporting Information. (c-e) magnetization saturation for x = 0.32, 0.40, and 0.46 samples. The dashed blue lines represent the magnetization saturation after removing the linear AFM magnetization background.

The emergence of a weak FM state at low temperatures is further illustrated by the field dependence of magnetization [$M(H)$] at T = 2 K shown in Figure 5. Because all samples show a symmetric response in the negative field as compared to the positive field scan (see Figure S3, Supporting Information), we depict $M(H)$ data from 0 to 9 T for all samples $0 \leq x \leq 1$ in Figure 5, and provided the low field magnetization in Figure S4 in Supporting Information to check possible magnetic hystersis. It has been reported that the end compounds $Ni_2P_2S_6$ and

$CuCrP_2S_6$ do not show magnetic hysteresis loops around zero field[70,71], consistent with their AFM ground states. Similarly, at low fields (Figure S4 in Supporting Information), magnetic hysteresis at $T = 2$ K is absent for compositions close to the end compounds, i.e. compositions in AFM_1 ($x \leq 0.32$) and AFM_2 ($x > 0.8$) regions. However, weak hysteresis at 2 K appears for $0.32 < x \leq 0.80$ in the in-plane magnetization measured with $H//ab$, consistent with the emergence of weak ferromagnetism at low temperatures for these intermediate compositions.

As shown in Figure 5a, in high Ni-content AFM_1 region, at $T = 2$ K, pristine $Ni_2P_2S_6$ displays a robust AFM ground state with linear field-dependent magnetization at low fields, which is followed by a metamagnetic transition around 6 T in in-plane magnetization that features a super-linear field dependence. Such a transition in $Ni_2P_2S_6$ has been attributed to a spin-flop transition in an antiferromagnet, which occurs with the magnetic field component along the magnetic easy axis[38], and hence the magnetization measure under the hard axis ($H \perp ab$) is featureless. For (Cu+Cr) co-substituted sample $x = 0.16$ belonging to the AFM_1 phase, in-plane magnetization also features a spin-flop transition but at a lower field around ~1 T, as indicated by the black arrow in the inset of Figure 5b. At the high field, sublinear magnetization is observed, without a clear sign of saturation up to 9 T. Increasing (Cu+Cr) compositions to 0.32, the spin-flop transition field is suppressed to around 0.15 T (Figure S5, supporting information). For the AFM_2 phase, i.e. high (Cu+Cr) content samples $x = 0.94$ and $x = 1$, spin-flop transition occurs around 0.3 T in $CuCrP_2S_6$ and 0.1 T in the $x = 0.16$ sample under in-plane field (Figure 5i and 5j, insets), followed by magnetization saturation above 6 T. On increasing substitution to the intermediate composition region, the spin-flop transition field is too low to be resolvable (Figure 5c-5h), consistent with the trend that the spin-flop field is suppressed with increasing substitution from either $Ni_2P_2S_6$ or $CuCrP_2S_6$ end compounds. Such suppression of the spin-flop field in intermediate compositions is expected, as the spin-flop field is related to

the magnetic exchange and anisotropy, whose combined effects lead to the strongly suppressed spin-flop field in the intermediate compositions, as discussed in the Supporting Information.

Despite the visible spin-flop transitions, in-plane magnetic easy axes for these intermediate compositions can be inferred from the fact that magnetization saturates quicker and reaches higher value under the in-plane field. The x = 0.32 sample (Figure 5c) exhibits moment polarization-like behavior at higher fields. Though a complete magnetization saturation is not achieved up to 9 T, given that the magnetization above 3 T displays a nearly linear field dependence, the saturation moment is estimated by subtracting such linear magnetization component. As shown by the dashed lines in the inset of Figure 5c, the magnetization saturation (M_{sat}) reaches ~(0.28±0.02)μ_B per f.u. Increasing (Cu+Cr) content to x = 0.40 which leads to stronger ZFC and FC irreversibility (Figure 4) and greater T_{irr} (Figure 3), a greater M_{sat} ~(0.38±0.03)μ_B per f.u. is observed (Figure 5d, inset), indicating stronger moment canting from x = 0.32 to 0.40 in the weak FM_1 phase regime.

The scenario becomes different in the weak FM_2 regime ($x \geq 0.46$). For the x = 0.46 sample, M_{sat} ~(0.86±0.04) μ_B is enhanced more than twice as compared to that of the x = 0.40 sample. Since the samples in this composition region are characterized by A-type AFM in this composition region (Figure 3), the stronger intra-layer FM correlation is likely to facilitate much stronger moment polarization. Further increasing (Cu+Cr) content leads to enhanced M_{sat}. For the end compound $CuCrP_2S_6$ which is characterized by a well-defined AFM state without the low-temperature weak FM_2 phase, the field-induced spin polarization leads to a substantial saturation moment of 2.79 μ_B, consistent with the reported value of 3.00 μ_B per f.u.[70].

Given that the weak FM_2 phase stems from the A-type AFM phase of the end compound $CuCrP_2S_6$, understanding the spin polarization of $CuCrP_2S_6$ may shed light on the saturation magnetization in doped samples. In $CuCrP_2S_6$, the moment saturation seen above ~6.5 T field has been attributed to the weak inter-layer AFM interaction for the A-type AFM ground state[70]. Therefore, for the doped sample x = 0.46 to 0.80 which exhibits the low-temperature weak FM_2

phase and is structurally similar to $CuCrP_2S_6$, the moment polarization is likely inherited from $CuCrP_2S_6$.

Figure 6 summarizes the observed saturation moment for $Cu_xNi_{2(1-x)}Cr_xP_2S_6$, together with the theoretical value $g_S S\mu_B$, where g_S (≈ 2) is Landé g-factor and $S = 1$ and 3/2 for Ni^{2+} and Cr^{3+} respectively. The observed $M_{sat} = 2.79\ \mu_B$ per f.u. in $CuCrP_2S_6$ is expected for Cr^{3+} ions. M_{sat} starts to deviate from the theoretical value upon substituting Ni in $CuCrP_2S_6$. The deviation becomes stronger with increasing Ni content (i.e., decreasing x value). Substituting 6% Ni in $CuCrP_2S_6$ ($x = 0.94$) reduces M_{sat} by nearly 24% of the theoretical value, which is surprising for such a low amount of Ni substitution and implies that each Ni moment prevents nearly three Cr moments from being polarized. Further increasing the Ni content leads to the greater suppression of M_{sat} in comparison to theoretical saturation magnetization, reaching only 12% of the theoretical value in the $x = 0.32$ sample, which is the boundary of the Weak FM_1 phase. For samples with higher Ni content ($x \leq 0.16$), magnetization saturation behavior is absent. Accompanied by the reducing saturation moment is the drop of magnetic field needed to induce the saturation ($\mu_0 H_{sat}$), as shown in the inset of Figure 6. Therefore, it appears that H_{sat} somewhat scales with the amount of Cr moments in this material system - more Cr moments require the higher field to polarize.

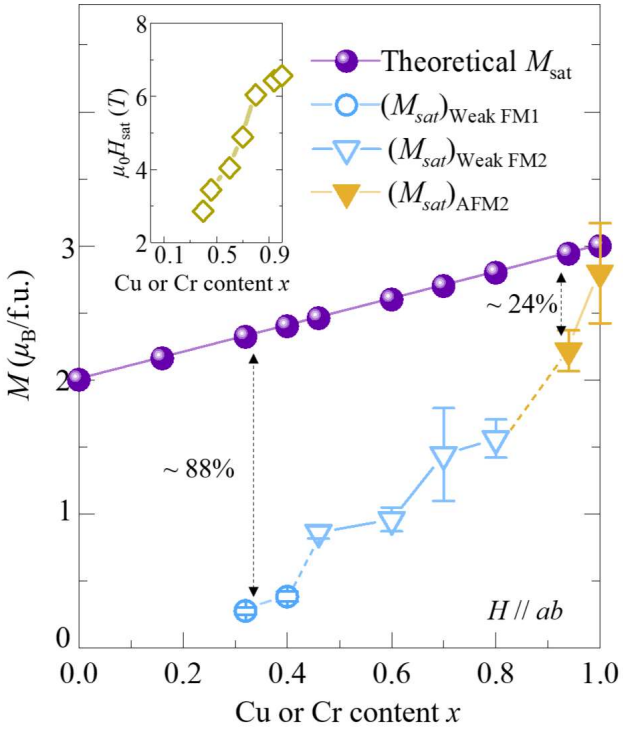

Figure 6. Doping dependence of saturated magnetization (M_{sat}) together with the theoretical M_{sat} values. The M_{sat} values for x = 0 and 0.16 samples are not shown because these samples lack magnetic saturation behavior up to magnetic field of 9 T. Inset: Doping dependence of saturation field ($\mu_0 H_{sat}$) for ferromagnetic-like polarization.

Similar partial moment polarization has also been reported in lightly Cr-substituted $Ni_2P_2S_6$[95]. Though only 9% Cr can be successfully induced in this bimetallic system, reduced moment and saturation fields have been observed. The tri-metallic system $Cu_xNi_{2(1-x)}Cr_xP_2S_6$ studied in this work greatly extends the doping level, demanding further in-depth experimental and theoretical investigations. Furthermore, the enhancement of saturation moment and the strengthening of FM correlations with (Cu+Cr) co-substitution in $Ni_2P_2S_6$ make this system promising for 2D magnetism studies. Directly probing AFM states in 2D layers can be challenging due to the lack of net magnetization. An earlier study has shown that the AFM order in $Ni_2P_2S_6$ remains stable down to the bilayer, though it disappears in the monolayer

limit[22]. In contrast, ferromagnetism has been observed in few-layer $CuCrP_2S_6$[110] and is predicted to persist in monolayer[111]. Although magnetic ordering in monolayer $CuCrP_2S_6$ remains undetermined, its A-type AFM structure - with FM coupled individual layers stacking antiferromagnetically[70,71] - suggests that ferromagnetism may persist to a single layer. Similarly, (Cu+Cr) co-substituted $Ni_2P_2S_6$, especially for the compositions within the Weak FM_1, Weak FM_2, and AFM_2 regimes, could exhibit FM correlations within each layer. In contrast, samples in the AFM_1 regime are more likely to retain AFM ordering akin to pristine $Ni_2P_2S_6$ even in the 2D limit. In addition to magnetism, the medium-entropy $Cu_xNi_{2(1-x)}Cr_xP_2S_6$ could be a promising material platform to study magneto-optics and magnetoelectric effects. One of the end compounds $Ni_2P_2S_6$ exhibits a strong coupling between magnetic order and light-matter interaction[41,112,113]. As discussed above, the (Cu+Cr) substitution in $Ni_2P_2S_6$ is highly efficient in tuning magnetic order and moment orientation, which could make unusual magneto-optical phenomena more accessible for novel photonic processes in layered magnets. Another end compound $CuCrP_2S_6$ displays interesting properties such as strong magnetoelectric coupling[97] and room-temperature ferroelectricity[114]. Thus, with the possible inheritance of these functionalities from the both end compounds, together with the tunable magnetism, would establish $Cu_xNi_{2(1-x)}Cr_xP_2S_6$ as a promising platform for developing multifunctional device applications.

3. Conclusion

In conclusion, we studied the magnetic properties of Cu, Cr, and Ni substituted medium-entropy compounds $Cu_xNi_{2(1-x)}Cr_xP_2S_6$ and found a systematic tuning of magnetism with substitution. The aliovalent (Cu+Cr) co-substitution for Ni induces a smooth evolution of AFM phases in contrast to magnetic frustration usually seen in conventional bimetallic substitutions. Increasing (Cu+Cr) contents also enhances FM correlation between magnetic moments, which is rare in previously reported $M_2P_2X_6$ compounds. These findings provide an interesting route

to investigate tunable magnetism in layered magnets as well as the study of magneto-optics, magnetoelectric effects, and other functional properties, which further extend the scope of 2D magnets beyond the fundamental studies towards the practical applications.

4. Experimental Section

$Cu_xNi_{2(1-x)}Cr_xP_2S_6$ ($0 \leq x \leq 1$) single crystals used in this work were synthesized by a chemical vapor transport method using I_2 as the transport agent. For each compositions except for $x = 1$, elemental powders with various ratios of Cu (99.9%, BeanTown Chemical): Ni (99.9%, BeanTown Chemical): Cr (99.9%, BeanTown Chemical): P (99.9%, BeanTown Chemical): S (99.9%, BeanTown Chemical) = x : 2(1-x) : x : 2: 6 were loaded in a quartz tube together with ~2 mg I_2. The tube was evacuated to a pressure ~10^{-3} Pa and sealed using an oxygen-hydrogen torch, heated in a two-zone furnace (Mellen TD) with a temperature gradient from 750 to 550 °C. For $CuCrP_2S_6$ (i.e., $x = 1$), however, higher temperatures are needed to ensure successful growth. This composition was synthesized using a different temperature gradient from 840 to 720 °C. Single crystals of millimeter size with flat and shiny surfaces can be obtained after one week of chemical vapor transport.

The elemental compositions were examined by the EDS at an accelerating voltage of 15 kV, using a FEI Nova Nanolab 200 dual beam workstation equipped with EDS, scanning electron microscopy, and focused ion beam. It is worth noting that the compositions determined by EDS deviate from the nominal compositions, as shown in Table 1. Furthermore, for the same nominal composition, the compositions of the obtained single crystals may vary from sample to sample, especially for the samples in the intermediate composition range. Nevertheless, though compositions are sample dependent, for each piece of crystal, the composition is homogeneous, as demonstrated by multiple EDS scans on different locations of the crystal. This ensures that the obtained properties for each composition are reliable. Therefore, it is crucial to use the crystals with well-characterized compositions for all experiments. From EDS

measurements, P and S contents deviate from stoichiometric values only by a few percent, which is common in EDS analysis due to instrumental limitations. In addition, the Cu and Cr contents are identical or only vary by a few percent from the exact 1:1 ratio. So a chemical formula of $Cu_xNi_{2(1-x)}Cr_xP_2S_6$, with x being the average composition of Cu or Cr, i.e., x= (Cu+Cr)/2, is used in this work.

The crystal structures of the obtained crystals were examined by powder XRD at room temperature using a Rigaku XtaLAB Synergy-S diffractometer. Owing to the variation of compositions in different pieces of crystals, crystals with well characterized compositions were grounded to power for XRD. Cross-sectional transmission electron microscopy samples were prepared using the in-situ lift-out technique in a FEI Nova Nanolab 200 duo-beam SEM/FIB. Cutting and polishing were achieved using a 30 keV Ga+ ion beam. The lamella was cut along a direction parallel to one of the crystal facets so that the electron beam may follow a low-indices direction. Imaging was performed in a FEI Titan 80-300 TEM fitted with an image Cs-corrector and operated at 300 kV. No damage or phase change were observed as the result of the high-energy electron beam exposure during the imaging.

Magnetization measurements up to 9 T were performed in a physical property measurement system (PPMS DynaCool, Quantum Design) using the ACMS II option which offers sensitivity of 5×10^{-6} emu for DC magnetic moment measurements. The magnetic property measurements were also performed in a 7 T magnetic property measurement system (MPMS3 SQUID, Quantum Design) which offers better resolution ($< 8\times10^{-8}$ emu) despite of lower magnetic field range. Consistent results were obtained from results obtained from PPMS DynaCool and MPMS3 SQUID.

Supporting Information

Supporting Information is available from the Wiley Online Library or from the author.

Acknowledgments

We acknowledge AFOSR award number FA9550-24-1-0263. Magnetization measurements using MPMS3 SQUID was supported by the MonArk NSF Quantum Foundry, National Science Foundation Q-AMASE-i program under award No. DMR-1906383. R.B, M.M.S, and M.M acknowledges μ-ATOMS, an Energy Frontier Research Center funded by DOE, Office of Science, Basic Energy Sciences, under Award No. DE-SC0023412 (structure determination and part of the magnetic property analysis). G.A is supported by National Science Foundation under Award DMR-2238254. J. S. acknowledges the support from NIH under award P20GM103429 for the powder XRD experiment.

Conflict of Interest

The authors declare no conflict of interest.

References

[1] G. Long, H. Henck, M. Gibertini, D. Dumcenco, Z. Wang, T. Taniguchi, K. Watanabe, E. Giannini, A. F. Morpurgo, *Nano Lett.* **2020**, *20*, 2452.

[2] Z. Wang, T. Zhang, M. Ding, B. Dong, Y. Li, M. Chen, X. Li, J. Huang, H. Wang, X. Zhao, Y. Li, D. Li, C. Jia, L. Sun, H. Guo, Y. Ye, D. Sun, Y. Chen, T. Yang, J. Zhang, S. Ono, Z. Han, Z. Zhang, *Nature Nanotechnology* **2018**, *13*, 554.

[3] B. Huang, G. Clark, D. R. Klein, D. MacNeill, E. Navarro-Moratalla, K. L. Seyler, N. Wilson, M. A. McGuire, D. H. Cobden, D. Xiao, W. Yao, P. Jarillo-Herrero, X. Xu, *Nature Nanotechnology* **2018**, *13*, 544.

[4] Y. Wang, J. Balgley, E. Gerber, M. Gray, N. Kumar, X. Lu, J.-Q. Yan, A. Fereidouni, R. Basnet, S. J. Yun, D. Suri, H. Kitadai, T. Taniguchi, K. Watanabe, X. Ling, J. Moodera, Y. H.

Lee, H. O. H. Churchill, J. Hu, L. Yang, E.-A. Kim, D. G. Mandrus, E. A. Henriksen, K. S. Burch, *Nano Lett.* **2020**, *20*, 8446.

[5] A. R. C. McCray, Y. Li, R. Basnet, K. Pandey, J. Hu, D. P. Phelan, X. Ma, A. K. Petford-Long, C. Phatak, *Nano Lett.* **2022**, *22*, 7804.

[6] J.-U. Lee, S. Lee, J. H. Ryoo, S. Kang, T. Y. Kim, P. Kim, C.-H. Park, J.-G. Park, H. Cheong, *Nano Lett.* **2016**, *16*, 7433.

[7] R. Basnet, J. Hu, *Nanoscale* **2024**, *16*, 15851.

[8] P. Witte, A. M. van Koten, M. E. Kamminga, *Materials Advances* **2024**, *5*, 6702.

[9] T. Masubuchi, X. Jin, K. Koyama, Y. Takahashi, K. Takase, Y. Uwatoko, Y. Takano, K. Sekizawa, *AIP Conference Proceedings* **2006**, *850*, 1279.

[10] T. Li, S. Jiang, N. Sivadas, Z. Wang, Y. Xu, D. Weber, J. E. Goldberger, K. Watanabe, T. Taniguchi, C. J. Fennie, K. Fai Mak, J. Shan, *Nat. Mater.* **2019**, *18*, 1303.

[11] S. Mondal, M. Kannan, M. Das, L. Govindaraj, R. Singha, B. Satpati, S. Arumugam, P. Mandal, *Phys. Rev. B* **2019**, *99*, 180407.

[12] Y. Peng, Z. Lin, G. Tian, J. Yang, P. Zhang, F. Wang, P. Gu, X. Liu, C.-W. Wang, M. Avdeev, F. Liu, D. Zhou, R. Han, P. Shen, W. Yang, S. Liu, Y. Ye, J. Yang, *Advanced Functional Materials* **2022**, *32*, 2106592.

[13] S. Jiang, L. Li, Z. Wang, K. F. Mak, J. Shan, *Nature Nanotechnology* **2018**, *13*, 549.

[14] Y. Zhou, D. Zhou, X. Jin, L. Zhang, X. Du, B. Li, *Sci Rep* **2018**, *8*, 1236.

[15] S. Singh, N. K. Katiyar, S. Goel, S. N. Joshi, *Sci Rep* **2023**, *13*, 4811.

[16] L. Min, M. Sretenovic, T. W. Heitmann, T. W. Valentine, R. Zu, V. Gopalan, C. M. Rost, X. Ke, Z. Mao, *Commun Phys* **2022**, *5*, 1.

[17] X. Chen, J. Wang, T. Ying, D. Huang, H. Gou, Q. Zhang, Y. Li, H. Hosono, J. Guo, X. Chen, *Phys. Rev. B* **2022**, *106*, 184502.

[18] T. Ying, T. Yu, Y.-S. Shiah, C. Li, J. Li, Y. Qi, H. Hosono, *J. Am. Chem. Soc.* **2021**, *143*, 7042.

[19] F. Wang, T. A. Shifa, P. Yu, P. He, Y. Liu, F. Wang, Z. Wang, X. Zhan, X. Lou, F. Xia, J. He, *Advanced Functional Materials* **2018**, *28*, 1802151.

[20] R. Samal, G. Sanyal, B. Chakraborty, C. S. Rout, *J. Mater. Chem. A* **2021**, *9*, 2560.

[21] M. A. Susner, M. Chyasnavichyus, M. A. McGuire, P. Ganesh, P. Maksymovych, *Advanced Materials* **2017**, *29*, 1602852.

[22] K. Kim, S. Y. Lim, J.-U. Lee, S. Lee, T. Y. Kim, K. Park, G. S. Jeon, C.-H. Park, J.-G. Park, H. Cheong, *Nature Communications* **2019**, *10*, 345.

[23] K. Kim, S. Y. Lim, J. Kim, J.-U. Lee, S. Lee, P. Kim, K. Park, S. Son, C.-H. Park, J.-G. Park, H. Cheong, *2D Mater.* **2019**, *6*, 041001.

[24] Z. Ni, A. V. Haglund, H. Wang, B. Xu, C. Bernhard, D. G. Mandrus, X. Qian, E. J. Mele, C. L. Kane, L. Wu, *Nat. Nanotechnol.* **2021**, *16*, 782.

[25] P. A. Joy, S. Vasudevan, *Phys. Rev. B* **1992**, *46*, 5425.

[26] A. R. Wildes, V. Simonet, E. Ressouche, G. J. Mcintyre, M. Avdeev, E. Suard, S. A. Kimber, D. Lançon, G. Pepe, B. Moubaraki, *Physical Review B* **2015**, *92*, 224408.

[27] K. C. Rule, G. J. McIntyre, S. J. Kennedy, T. J. Hicks, *Phys. Rev. B* **2007**, *76*, 134402.

[28] A. R. Wildes, H. M. Rønnow, B. Roessli, M. J. Harris, K. W. Godfrey, *Phys. Rev. B* **2006**, *74*, 094422.

[29] D. Lançon, H. C. Walker, E. Ressouche, B. Ouladdiaf, K. C. Rule, G. J. McIntyre, T. J. Hicks, H. M. Rønnow, A. R. Wildes, *Phys. Rev. B* **2016**, *94*, 214407.

[30] A. R. Wildes, B. Roessli, B. Lebech, K. W. Godfrey, *J. Phys.: Condens. Matter* **1998**, *10*, 6417.

[31] A. R. Wildes, V. Simonet, E. Ressouche, R. Ballou, G. J. McIntyre, *J. Phys.: Condens. Matter* **2017**, *29*, 455801.

[32] T. Sekine, M. Jouanne, C. Julien, M. Balkanski, *Phys. Rev. B* **1990**, *42*, 8382.

[33] Y. Takano, N. Arai, A. Arai, Y. Takahashi, K. Takase, K. Sekizawa, *Journal of Magnetism and Magnetic Materials* **2004**, *272–276*, E593.

[34] G. Long, T. Zhang, X. Cai, J. Hu, C. Cho, S. Xu, J. Shen, Z. Wu, T. Han, J. Lin, J. Wang, Y. Cai, R. Lortz, Z. Mao, N. Wang, *ACS Nano* **2017**, *11*, 11330.

[35] D. J. Goossens, T. J. Hicks, *J. Phys.: Condens. Matter* **1998**, *10*, 7643.

[36] K. Okuda, K. Kurosawa, S. Saito, M. Honda, Z. Yu, M. Date, *J. Phys. Soc. Jpn.* **1986**, *55*, 4456.

[37] D. J. Goossens, A. R. Wildes, C. Ritter, T. J. Hicks, *J. Phys.: Condens. Matter* **2000**, *12*, 1845.

[38] R. Basnet, A. Wegner, K. Pandey, S. Storment, J. Hu, *Phys. Rev. Materials* **2021**, *5*, 064413.

[39] A. R. Wildes, D. Lançon, M. K. Chan, F. Weickert, N. Harrison, V. Simonet, M. E. Zhitomirsky, M. V. Gvozdikova, T. Ziman, H. M. Rønnow, *Phys. Rev. B* **2020**, *101*, 024415.

[40] Y. Shemerliuk, Y. Zhou, Z. Yang, G. Cao, A. U. B. Wolter, B. Büchner, S. Aswartham, *Electronic Materials* **2021**, *2*, 284.

[41] D. Afanasiev, J. R. Hortensius, M. Matthiesen, S. Mañas-Valero, M. Šiškins, M. Lee, E. Lesne, H. S. J. van der Zant, P. G. Steeneken, B. A. Ivanov, E. Coronado, A. D. Caviglia, *Science Advances 7*, eabf3096.

[42] A. Wiedenmann, J. Rossat-Mignod, A. Louisy, R. Brec, J. Rouxel, *Solid State Communications* **1981**, *40*, 1067.

[43] A. H. Thompson, M. S. Whittingham, *Materials Research Bulletin* **1977**, *12*, 741.

[44] P. J. S. Foot, T. Katz, S. N. Patel, B. A. Nevett, A. R. Pieecy, A. A. Balchin, *Phys. Stat. Sol. (a)* **1987**, *100*, 11.

[45] J. Yang, Y. Zhou, Y. Dedkov, E. Voloshina, *Advanced Theory and Simulations* **2020**, *3*, 2000228.

[46] B. L. Chittari, Y. Park, D. Lee, M. Han, A. H. MacDonald, E. Hwang, J. Jung, *Phys. Rev. B* **2016**, *94*, 184428.

[47] N. Chandrasekharan, S. Vasudevan, *Phys. Rev. B* **1996**, *54*, 14903.

[48] D. J. Goossens, A. J. Studer, S. J. Kennedy, T. J. Hicks, *J. Phys.: Condens. Matter* **2000**, *12*, 4233.

[49] A. M. Mulders, J. C. P. Klaasse, D. J. Goossens, J. Chadwick, T. J. Hicks, *J. Phys.: Condens. Matter* **2002**, *14*, 8697.

[50] Y. Takano, A. Arai, Y. Takahashi, K. Takase, K. Sekizawa, *Journal of Applied Physics* **2003**, *93*, 8197.

[51] J. N. Graham, M. J. Coak, S. Son, E. Suard, J.-G. Park, L. Clark, A. R. Wildes, *Phys. Rev. Materials* **2020**, *4*, 084401.

[52] T. Masubuchi, H. Hoya, T. Watanabe, Y. Takahashi, S. Ban, N. Ohkubo, K. Takase, Y. Takano, *Journal of Alloys and Compounds* **2008**, *460*, 668.

[53] V. Manríquez, P. Barahona, O. Peña, *Materials Research Bulletin* **2000**, *35*, 1889.

[54] D. J. Goossens, S. Brazier-Hollins, D. R. James, W. D. Hutchison, J. R. Hester, *Journal of Magnetism and Magnetic Materials* **2013**, *334*, 82.

[55] Y. He, Y.-D. Dai, H. Huang, J. Lin, Y. Hsia, *Journal of Alloys and Compounds* **2003**, *359*, 41.

[56] A. Bhutani, J. L. Zuo, R. D. McAuliffe, C. R. dela Cruz, D. P. Shoemaker, *Phys. Rev. Materials* **2020**, *4*, 034411.

[57] S. Selter, Y. Shemerliuk, M.-I. Sturza, A. U. B. Wolter, B. Büchner, S. Aswartham, *Phys. Rev. Materials* **2021**, *5*, 073401.

[58] F. Wang, N. Mathur, A. N. Janes, H. Sheng, P. He, X. Zheng, P. Yu, A. J. DeRuiter, J. R. Schmidt, J. He, S. Jin, *Science Advances 7*, eabj4086.

[59] S. Lee, J. Park, Y. Choi, K. Raju, W.-T. Chen, R. Sankar, K.-Y. Choi, *Phys. Rev. B* **2021**, *104*, 174412.

[60] J. P. Odile, J. J. Steger, Aaron. Wold, *Inorg. Chem.* **1975**, *14*, 2400.

[61] S. Calder, A. V. Haglund, A. I. Kolesnikov, D. Mandrus, *Phys. Rev. B* **2021**, *103*, 024414.

[62] P. Jeevanandam, S. Vasudevan, *J. Phys.: Condens. Matter* **1999**, *11*, 3563.

[63] R. Basnet, K. M. Kotur, M. Rybak, C. Stephenson, S. Bishop, C. Autieri, M. Birowska, J. Hu, *Phys. Rev. Research* **2022**, *4*, 023256.

[64] H. Han, H. Lin, W. Gan, Y. Liu, R. Xiao, L. Zhang, Y. Li, C. Zhang, H. Li, *Appl. Phys. Lett.* **2023**, *122*, 033101.

[65] D. Tezze, J. M. Pereira, Y. Asensio, M. Ipatov, F. Calavalle, F. Casanova, A. M. Bittner, M. Ormaza, B. Martín-García, L. E. Hueso, M. Gobbi, *Nanoscale* **2022**, *14*, 1165.

[66] M. Mi, X. Zheng, S. Wang, Y. Zhou, L. Yu, H. Xiao, H. Song, B. Shen, F. Li, L. Bai, Y. Chen, S. Wang, X. Liu, Y. Wang, *Advanced Functional Materials* **2022**, *32*, 2112750.

[67] R. Basnet, D. Ford, K. TenBarge, J. Lochala, J. Hu, *J. Phys.: Condens. Matter* **2022**, *34*, 434002.

[68] D. Upreti, R. Basnet, M. M. Sharma, S. K. Chhetri, G. Acharya, M. R. U. Nabi, J. Sakon, B. Da, M. Mortazavi, J. Hu, *Tuning Magnetism in Ising-type van der Waals Magnet FePS3 by Lithium Intercalation*, arXiv, **2024**.

[69] J. Peng, X. Yang, Z. Lu, L. Huang, X. Chen, M. He, J. Shen, Y. Xing, M. Liu, Z. Qu, Z. Wang, L. Li, S. Dong, J.-M. Liu, *Advanced Quantum Technologies* **2023**, *6*, 2200105.

[70] S. Selter, K. K. Bestha, P. Bhattacharyya, B. Özer, Y. Shemerliuk, M. Roslova, E. Vinokurova, L. T. Corredor, L. Veyrat, A. U. B. Wolter, L. Hozoi, B. Büchner, S. Aswartham, *Phys. Rev. Mater.* **2023**, *7*, 033402.

[71] X. Wang, Z. Shang, C. Zhang, J. Kang, T. Liu, X. Wang, S. Chen, H. Liu, W. Tang, Y.-J. Zeng, J. Guo, Z. Cheng, L. Liu, D. Pan, S. Tong, B. Wu, Y. Xie, G. Wang, J. Deng, T. Zhai, H.-X. Deng, J. Hong, J. Zhao, *Nat Commun* **2023**, *14*, 840.

[72] C. Payen, H. Mutka, J. L. Soubeyroux, P. Molinié, P. Colombet, *Journal of Magnetism and Magnetic Materials* **1992**, *104–107*, 797.

[73] S. Selter, Y. Shemerliuk, B. Büchner, S. Aswartham, *Crystals* **2021**, *11*, 500.

[74] H. Mutka, C. Payen, P. Molinié, J. L. Soubeyroux, P. Colombet, A. D. Taylor, *Phys. Rev. Lett.* **1991**, *67*, 497.

[75] P. Colombet, A. Leblanc, M. Danot, J. Rouxel, *Journal of Solid State Chemistry* **1982**, *41*, 174.

[76] S. Lee, P. Colombet, G. Ouvrard, R. Brec, *Materials Research Bulletin* **1986**, *21*, 917.

[77] Y. Peng, X. Cheng, P. Gu, F. Wang, J. Yang, M. Xue, W. Yang, C. Wang, S. Liu, K. Watanabe, T. Taniguchi, Y. Ye, J. Yang, *Advanced Functional Materials* **2020**, *30*, 1910036.

[78] M. A. Susner, B. S. Conner, E. Rowe, R. Siebenaller, A. Giordano, M. V. McLeod, C. R. Ebbing, T. J. Bullard, R. Selhorst, T. J. Haugan, J. Jiang, R. Pachter, R. Rao, *J. Phys. Chem. C* **2024**.

[79] M. A. McGuire, G. Clark, S. KC, W. M. Chance, G. E. Jellison, V. R. Cooper, X. Xu, B. C. Sales, *Phys. Rev. Mater.* **2017**, *1*, 014001.

[80] Y. Peng, S. Ding, M. Cheng, Q. Hu, J. Yang, F. Wang, M. Xue, Z. Liu, Z. Lin, M. Avdeev, Y. Hou, W. Yang, Y. Zheng, J. Yang, *Advanced Materials* **2020**, *32*, 2001200.

[81] E. J. Telford, A. H. Dismukes, K. Lee, M. Cheng, A. Wieteska, A. K. Bartholomew, Y.-S. Chen, X. Xu, A. N. Pasupathy, X. Zhu, C. R. Dean, X. Roy, *Advanced Materials* **2020**, *32*, 2003240.

[82] B. Kuhlow, *physica status solidi (a)* **1982**, *72*, 161.

[83] J. W. Cable, M. K. Wilkinson, E. O. Wollan, *Journal of Physics and Chemistry of Solids* **1961**, *19*, 29.

[84] B. Huang, G. Clark, E. Navarro-Moratalla, D. R. Klein, R. Cheng, K. L. Seyler, D. Zhong, E. Schmidgall, M. A. McGuire, D. H. Cobden, W. Yao, D. Xiao, P. Jarillo-Herrero, X. Xu, *Nature* **2017**, *546*, 270.

[85] C. Gong, L. Li, Z. Li, H. Ji, A. Stern, Y. Xia, T. Cao, W. Bao, C. Wang, Y. Wang, Z. Q. Qiu, R. J. Cava, S. G. Louie, J. Xia, X. Zhang, *Nature* **2017**, *546*, 265.

[86] A. Bedoya-Pinto, J.-R. Ji, A. K. Pandeya, P. Gargiani, M. Valvidares, P. Sessi, J. M. Taylor, F. Radu, K. Chang, S. S. P. Parkin, *Science* **2021**, *374*, 616.

[87] X. Cai, T. Song, N. P. Wilson, G. Clark, M. He, X. Zhang, T. Taniguchi, K. Watanabe, W. Yao, D. Xiao, M. A. McGuire, D. H. Cobden, X. Xu, *Nano Lett.* **2019**, *19*, 3993.

[88] J. Son, S. Son, P. Park, M. Kim, Z. Tao, J. Oh, T. Lee, S. Lee, J. Kim, K. Zhang, K. Cho, T. Kamiyama, J. H. Lee, K. F. Mak, J. Shan, M. Kim, J.-G. Park, J. Lee, *ACS Nano* **2021**, *15*, 16904.

[89] M. Baithi, N. T. Dang, T. A. Tran, J. P. Fix, D. H. Luong, K. P. Dhakal, D. Yoon, A. V. Rutkauskas, S. E. Kichanov, I. Y. Zel, J. Kim, N. J. Borys, D. P. Kozlenko, Y. H. Lee, D. L. Duong, *Inorg. Chem.* **2023**, *62*, 12674.

[90] Z.-L. Huang, J.-T. Zhao, J.-X. Mi, S.-Y. Mao, L.-S. Zheng, *Journal of Solid State Chemistry* **1999**, *144*, 388.

[91] D. Sen, T. Saha-Dasgupta, *Phys. Rev. Mater.* **2023**, *7*, 064008.

[92] G. Ouvrard, R. Fréour, R. Brec, J. Rouxel, *Materials Research Bulletin* **1985**, *20*, 1053.

[93] K. Ichimura, M. Sano, *Synthetic Metals* **1991**, *45*, 203.

[94] M. J. Coak, S. Son, D. Daisenberger, H. Hamidov, C. R. S. Haines, P. L. Alireza, A. R. Wildes, C. Liu, S. S. Saxena, J.-G. Park, *npj Quantum Materials* **2019**, *4*, 1.

[95] R. Basnet, D. Upreti, T. Patel, S. Karki Chhetri, G. Acharya, M. R. U. Nabi, M. M. Sharma, J. Sakon, M. Mortazavi, J. Hu, *Phys. Rev. B* **2024**, *109*, 184405.

[96] D. J. Goossens, D. James, J. Dong, R. E. Whitfield, L. Norén, R. L. Withers, *J. Phys.: Condens. Matter* **2011**, *23*, 065401.

[97] C. B. Park, A. Shahee, K.-T. Kim, D. R. Patil, S. A. Guda, N. Ter-Oganessian, K. H. Kim, *Advanced Electronic Materials* **2022**, *8*, 2101072.

[98] V. Maisonneuve, C. Payen, V. B. Cajipe, *Journal of Solid State Chemistry* **1995**, *116*, 208.

[99] R. Zhang, S. Zhao, J. Ding, Y. Chong, T. Jia, C. Ophus, M. Asta, R. O. Ritchie, A. M. Minor, *Nature* **2020**, *581*, 283.

[100] J. Ding, Q. Yu, M. Asta, R. O. Ritchie, *Proceedings of the National Academy of Sciences* **2018**, *115*, 8919.

[101] D. Lançon, R. A. Ewings, T. Guidi, F. Formisano, A. R. Wildes, *Phys. Rev. B* **2018**, *98*, 134414.

[102] A. R. Wildes, J. R. Stewart, M. D. Le, R. A. Ewings, K. C. Rule, G. Deng, K. Anand, *Phys. Rev. B* **2022**, *106*, 174422.

[103] Z. Lu, X. Yang, L. Huang, X. Chen, M. Liu, J. Peng, S. Dong, J.-M. Liu, *J. Phys.: Condens. Matter* **2022**, *34*, 354005.

[104] R. Basnet, T. Patel, J. Wang, D. Upreti, S. K. Chhetri, G. Acharya, M. R. U. Nabi, J. Sakon, J. Hu, *Advanced Electronic Materials* **2024**, *10*, 2300738.

[105] H. Han, H. Lin, W. Gan, R. Xiao, Y. Liu, J. Ye, L. Chen, W. Wang, L. Zhang, C. Zhang, H. Li, *Phys. Rev. B* **2023**, *107*, 075423.

[106] R. M. Bozorth, *Phys. Rev. Lett.* **1958**, *1*, 362.

[107] D. Treves, *Phys. Rev.* **1962**, *125*, 1843.

[108] V. V. Mazurenko, V. I. Anisimov, *Phys. Rev. B* **2005**, *71*, 184434.

[109] C. Autieri, R. M. Sattigeri, G. Cuono, A. Fakhredine, *Staggered Dzyaloshinskii-Moriya inducing weak ferromagnetism in centrosymmetric altermagnets and weak ferrimagnetism in noncentrosymmetric altermagnets*, arXiv, **2024**.

[110] Y. Lai, Z. Song, Y. Wan, M. Xue, C. Wang, Y. Ye, L. Dai, Z. Zhang, W. Yang, H. Du, J. Yang, *Nanoscale* **2019**, *11*, 5163.

[111] J. Qi, H. Wang, X. Chen, X. Qian, *Applied Physics Letters* **2018**, *113*, 043102.

[112] S. Kang, K. Kim, B. H. Kim, J. Kim, K. I. Sim, J.-U. Lee, S. Lee, K. Park, S. Yun, T. Kim, A. Nag, A. Walters, M. Garcia-Fernandez, J. Li, L. Chapon, K.-J. Zhou, Y.-W. Son, J. H. Kim, H. Cheong, J.-G. Park, *Nature* **2020**, *583*, 785.

[113] X. Wang, J. Cao, Z. Lu, A. Cohen, H. Kitadai, T. Li, Q. Tan, M. Wilson, C. H. Lui, D. Smirnov, S. Sharifzadeh, X. Ling, *Nat. Mater.* **2021**, *20*, 964.

[114] W. F. Io, S.-Y. Pang, L. W. Wong, Y. Zhao, R. Ding, J. Mao, Y. Zhao, F. Guo, S. Yuan, J. Zhao, J. Yi, J. Hao, *Nat Commun* **2023**, *14*, 7304.